



Observation of single-defect memristor in an MoS₂ atomic sheet

Saban M. Hus¹, Ruijing Ge², Po-An Chen³, Liangbo Liang⁴, Gavin E. Donnelly⁵, Wonhee Ko⁴, Fumin Huang⁵, Meng-Hsueh Chiang³, An-Ping Li⁴ and Deji Akinwande^{1,2}✉

Non-volatile resistive switching, also known as memristor¹ effect, where an electric field switches the resistance states of a two-terminal device, has emerged as an important concept in the development of high-density information storage, computing and reconfigurable systems^{2–9}. The past decade has witnessed substantial advances in non-volatile resistive switching materials such as metal oxides and solid electrolytes. It was long believed that leakage currents would prevent the observation of this phenomenon for nanometre-thin insulating layers. However, the recent discovery of non-volatile resistive switching in two-dimensional monolayers of transition metal dichalcogenide^{10,11} and hexagonal boron nitride¹² sandwich structures (also known as atomristors) has refuted this belief and added a new materials dimension owing to the benefits of size scaling^{10,13}. Here we elucidate the origin of the switching mechanism in atomic sheets using monolayer MoS₂ as a model system. Atomistic imaging and spectroscopy reveal that metal substitution into a sulfur vacancy results in a non-volatile change in the resistance, which is corroborated by computational studies of defect structures and electronic states. These findings provide an atomistic understanding of non-volatile switching and open a new direction in precision defect engineering, down to a single defect, towards achieving the smallest memristor for applications in ultra-dense memory, neuromorphic computing and radio-frequency communication systems^{2,3,11}.

With a combination of scanning tunnelling microscopy/scanning tunnelling spectroscopy (STM/STS) and local transport studies, we observe that the sulfur vacancy, which is the predominant defect in MoS₂ monolayers, does not serve as a low-resistance path in its native form, in stark contrast to the effect of oxygen vacancies in a metal-oxide memory. However, metal ions, such as gold ions, migrating from the bottom or top electrodes can be substituted into the sulfur vacancy, resulting in a conducting local density of states (LDOS), which drives the atomic sheet to a low resistive state. After the removal of the gold atom under a reverse electric field, defects recover their initial vacancy structure and the system returns to a high resistive state. This conductive-point switching mechanism resembles the formation of a conductive bridge memory¹⁴ at an atomic level. However, it is fundamentally different and unique as a single metal ion fills a single vacancy site in a crystalline lattice rather than forming a metal bridge through a highly disordered material. We found that the sulfur vacancies are stable at a 2 nm pitch, resulting in a memristor density of approximately 1 unit per

4 nm² (25 Tbit cm^{−2}) with a cross-section of ~1 nm² for an individual defect. Furthermore, with the precise control of defects and substitution metal, the performance parameters, such as speed, energy, retention and endurance, can be tailored and new functionalities vis-à-vis a magnetic metal or reactive metal can be conferred.

MoS₂ monolayers were prepared by exfoliation onto freshly deposited gold surfaces using a previously described gold-assisted mechanical exfoliation technique¹⁵ that yields large-area monolayers (Fig. 1a). The gold underlayer served both as a conductive substrate for STM investigations and as a bottom electrode for in situ transport studies. Large-scale STM images (Fig. 1b and Supplementary Fig. 1) show continuous MoS₂ monolayers that seamlessly cover the terraces and step edges of the underlying gold surface. Raman and photoluminescence (PL) spectra of the MoS₂ flakes are consistent with the characteristics of monolayer MoS₂, as shown in Fig. 1c,d, respectively¹⁵. In these spectra, the broadening of the PL peak can be ascribed to the variations in the local strain caused by the relative crystal orientation of the underlying gold surface and MoS₂ monolayer^{15,16} and variations in the interface between the two. Furthermore, the PL signal is dominated by regions with weak Au–MoS₂ interaction as the signal is quenched in the regions with a strong interaction.

All the exfoliated films were annealed at 250 °C for several hours in ultrahigh vacuum conditions before the initial STM investigations. These mildly annealed samples exhibit a hexagonal lattice of 0.32 ± 0.02 nm periodicity of atomically clean MoS₂ surface with a very low native defect density (Fig. 2a). However, after annealing the samples at 400 °C, a large number of defects (of the order of 10¹³ cm^{−2}) centred around the sulfur atom positions are observed (Fig. 2b). The dominant defects have been identified as sulfur monovacancies^{17,18} (V_S), which are known to be the most common in both exfoliated and synthesized MoS₂ monolayers¹⁹ due to their low formation energy.

STS measurements on the defect-free regions (Fig. 2c and Supplementary Fig. 2) show a bandgap of ~1.4 eV, which is considerably lower than the optical bandgap (~1.8 eV) of monolayer MoS₂ and the bandgap values obtained from the STS measurements of the MoS₂ monolayer on highly oriented pyrolytic graphite²⁰. This reduction in the bandgap has been previously observed and attributed to charge transfer from the gold substrate^{21,22}. While the V_S defects are expected to introduce in-gap states¹⁷, STS measurements with stabilization voltages outside the bandgap do not reveal the in-gap states and do not show a clear bandgap difference between the defect-free regions and defect locations. However, the STS spectra taken with

¹Electrical and Computer Engineering, The University of Texas at Austin, Austin, TX, USA. ²Texas Materials Institute, The University of Texas at Austin, Austin, TX, USA. ³Institute of Microelectronics, Department of Electrical Engineering, National Cheng Kung University, Tainan, Taiwan. ⁴Center for Nanophase Materials Sciences, Oak Ridge National Laboratory, Oak Ridge, TN, USA. ⁵School of Mathematics and Physics, Queen's University Belfast, Belfast, UK. ✉e-mail: deji@ece.utexas.edu

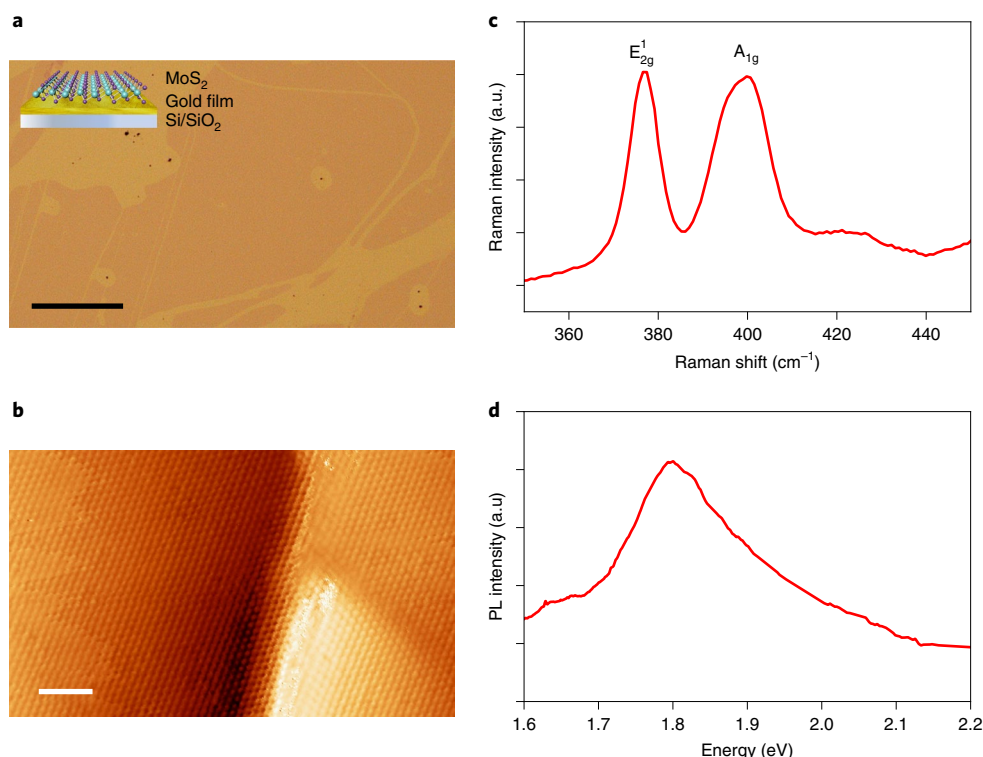


Fig. 1 | Material characterization. **a**, Optical image of exfoliated large-area monolayer MoS₂ flakes on a gold thin film. Scale bar, 100 μ m. Inset: schematic of the structure. **b**, STM image showing large, defect-free MoS₂ monolayers covering the terrace and step edges of the underlying gold film. Scale bar, 2 nm. **c**, Raman spectra of monolayer MoS₂ flakes, showing the main in-plane (E_{2g}^1) and out-of-plane (A_{1g}) vibrational modes. **d**, PL spectrum.

stabilization voltages within the bandgap ($V_{\text{sample}} = -1.0$ V) enable the observation of in-gap states (Supplementary Fig. 3a). When a smaller stabilization voltage ($V_{\text{sample}} = -0.5$ V) is used, the tunnelling principally occurs between the tip and the gold substrate, and the electronic states of the gold surface can be identified^{23,24}. In this case, the STS spectra measured at the defect-free regions and near the defects become identical again (Supplementary Fig. 3b). These measurements reveal that V_s defects do not enhance the tunnelling current through the MoS₂ monolayers or act like conductive filaments in their original configuration.

Conventional STS measurements provide useful transport information through atomically thin layers. However, the current density is limited due to the high tunnelling resistance of the vacuum gap between the STM tip and the sample surface, which may hinder the physical processes that normally occur in vertical metal–insulator–metal (MIM) devices. To better replicate the MIM device structure and investigate the non-volatile resistive switching effect at the atomic scale, we employed a gold STM tip as the top electrode for transport measurements. The STM tip was fixed on the surface with a stabilization voltage within the bandgap and was further moved towards the MoS₂ surface for 2–4 Å to form a stable physical contact. Then, d.c. electrical measurements were performed on this device configuration by sweeping the tip bias.

Transport measurements on the defect-free regions reveal a tunnelling-like current–voltage (I – V) behaviour for low bias voltages (Fig. 2d). The I – V curves are asymmetric around the zero bias as a result of the two different contact geometries of the bottom and top electrodes (flat gold film versus sharp gold STM tip). Using the same tip and repeating the transport measurements around the defect sites reveal unipolar diode-like behaviour with suppressed charge transport for positive tip biases (Fig. 2e), possibly due to charge accumulation²⁵ or tip-induced modification of the band

structure²⁶ around the defect sites. With further tip approaches, the I – V curves become more symmetric for both defect-free regions and at the defect positions (Supplementary Fig. 4), suggesting a flatter and larger contact between the STM tip and MoS₂ surface covering the pristine regions around the defects. STM imaging after these transport measurements do not present any visible modification of the MoS₂ surface, confirming the generally non-invasive character of the low-bias transport measurements with gold STM tips.

While most transport measurements do not alter the MoS₂ surface and return I – V curves similar to those shown in Fig. 2d,e, occasionally, I – V curves that resemble resistive switching events between a high resistance value of 2.5 G Ω and a low resistance value of 110 M Ω can be observed at the defect location (Fig. 2f). Although it is enticing to associate these events to the modifications of the tip apex, we note that such resistive switching events have never been observed on defect-free MoS₂ regions, directly establishing a connection between the sulfur vacancy defects and switching events. STM images before and after such switching events (Supplementary Fig. 5) indicate that the switching events can initiate the formation of new defects and modifications on the terrace structure of the gold substrate.

In addition, STM investigations reveal a second type of defect, which presents triangular symmetry (Fig. 3a) with darker contrast than the nearby V_s defects and are recognized as a sulfur divacancy²⁷ (V_{s2}), the second most common defect in exfoliated MoS₂ monolayers with a V_s : V_{s2} defect ratio of ~ 10 :1 (ref. ²⁸). Similar to V_s defects, STS measurements on the V_{s2} defect sites show a bandgap virtually identical to those of defect-free regions, as shown in Fig. 3f. When the transport measurements described above are repeated on the V_{s2} defect sites, a switching behaviour (a ‘set’ event from high to low resistance state) can be triggered at a tip bias of ~ 1.8 V, where a discontinuity is observed in the I – V curves (Fig. 3b). After the

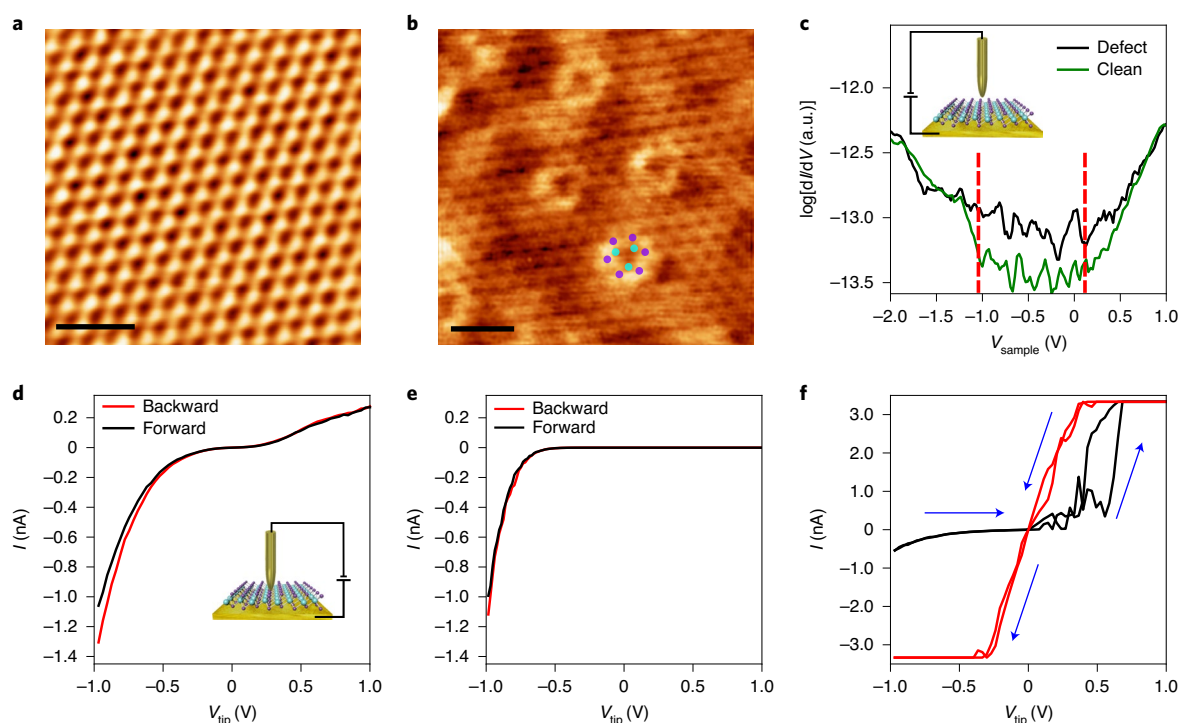


Fig. 2 | Atomistic characterization of MoS₂ monolayers. **a**, Atomically resolved STM image of exfoliated monolayer MoS₂ on a gold film showing the defect-free regions. Scale bar, 1 nm. **b**, V_S defects whose density can be increased by vacuum annealing (of the order of 10¹³ cm⁻²). Locations of sulfur and molybdenum atoms are shown in purple and cyan, respectively. The distance between the defects is ~2 nm. Scale bar, 1 nm. **c**, The dI/dV spectrum taken from a defect-free region is shown in green, while the one taken from and around the defects is shown in black (V_{sample} = -2.5 V; I = 100 pA). The red dashed lines are guides for the eye to indicate the bandgap. Inset: schematic of the STM/STS measurements with a vacuum gap for the imaging and spectroscopy measurements. **d**, Representative I-V curves for the transport measurements on defect-free regions, which presents an asymmetric diode-like behaviour. Inset: schematic of the transport measurements with a gold STM tip mimicking an atomic-scale MIM device structure. **e**, Unipolar diode-like I-V curves representing the majority of transport measurements on the V_S defect sites. **f**, Resistive switching events observed at two different defect locations during the transport measurements.

current reaches the compliance limit (330 nA), the bias is decreased, and hysteresis is observed in the I-V curves. STM images taken at the same location after the switching event show that the dark spot is replaced by a bright protrusion of ~0.5 Å height (Fig. 3c and Supplementary Fig. 6). The stability and height of the bright spot indicate that the vacancy defect has been occupied by a substituent atom. STS measurements at the bright spot show a non-zero density of states at the Fermi level, revealing the metallic characteristics of the defect site (Fig. 3f). Furthermore, the transport data at low bias voltages indicate that the zero-bias resistance decreases from 225 to 50 MΩ. While the measured on/off ratio is relatively small compared with larger micrometre devices¹⁰, it should be noted that the resistance of the atomic-scale contact between the STM tip and the defect site, that is, the contact resistance, probably plays a role in diminishing the intrinsic on/off ratio. Nevertheless, for practical consideration, there are additional degrees of freedom available for device engineering to improve the on/off ratio, such as the choice of metal electrode and the use of higher bandgap monolayers (for example, WS₂ (ref. ¹⁰) or hexagonal boron nitride (ref. ¹²)). First-principles calculation based on the density functional theory for Au-MoS₂-Au atomistic models and non-equilibrium Green's function for transport reveal that gold-ion adsorption into a staggered divacancy results in a noticeable change in the current (Supplementary Fig. 7), which is consistent with the experimental observations. Subsequent transport measurements with an opposite tip bias trigger a second resistive switching event from low to high resistance (the 'reset' event) at the same defect site where the resistance sharply increases at a tip bias of approximately -1.1 V

(Fig. 3d). Subsequent STM imaging data at the same location show that the defect returns to its original vacancy state after the reset event (Fig. 3e).

To elucidate the nature of the defect before and after the switching event, we compared the measured STM dI/dV spectra with the calculated LDOS for an agglomerated V_{S2} vacancy on the opposite sides of the MoS₂ monolayer and with defect structures where the top sulfur vacancy of the V_{S2} complex is substituted with the gold atom. The simulated STM images (Fig. 4) qualitatively match the experimental STM images with the V_{S2} defects, presenting a much higher contrast than V_S, and gold substitution showing a bright protrusion at the centre of the defect site. Importantly, the LDOS calculations (Fig. 4 and Supplementary Fig. 8) show finite electronic states around the Fermi level after gold substitution in both V_S and V_{S2} defects, indicating a metallic-like behaviour near these gold absorption sites, which were initially insulating. These calculation results corroborate the experimental observations according to which gold substitution at the defect site by a positive electric field introduces conducting electronic states around the Fermi level to reduce the resistance, while gold removal from the defect site by an opposite field returns the system to its insulating state.

Formation energies of the defect structures are critical for determining the stability of these defects and the transitions between them. In MoS₂ monolayers, the formation energy for the V_S (V_{S2}) vacancy varies between 1.3 to 2.9 eV (2.9 to 5.9 eV) for the Mo-rich and S-rich limit, respectively (Supplementary Fig. 9). While these defect sites are expected to be stable at room temperature and under standard STM imaging conditions, due to their relatively low

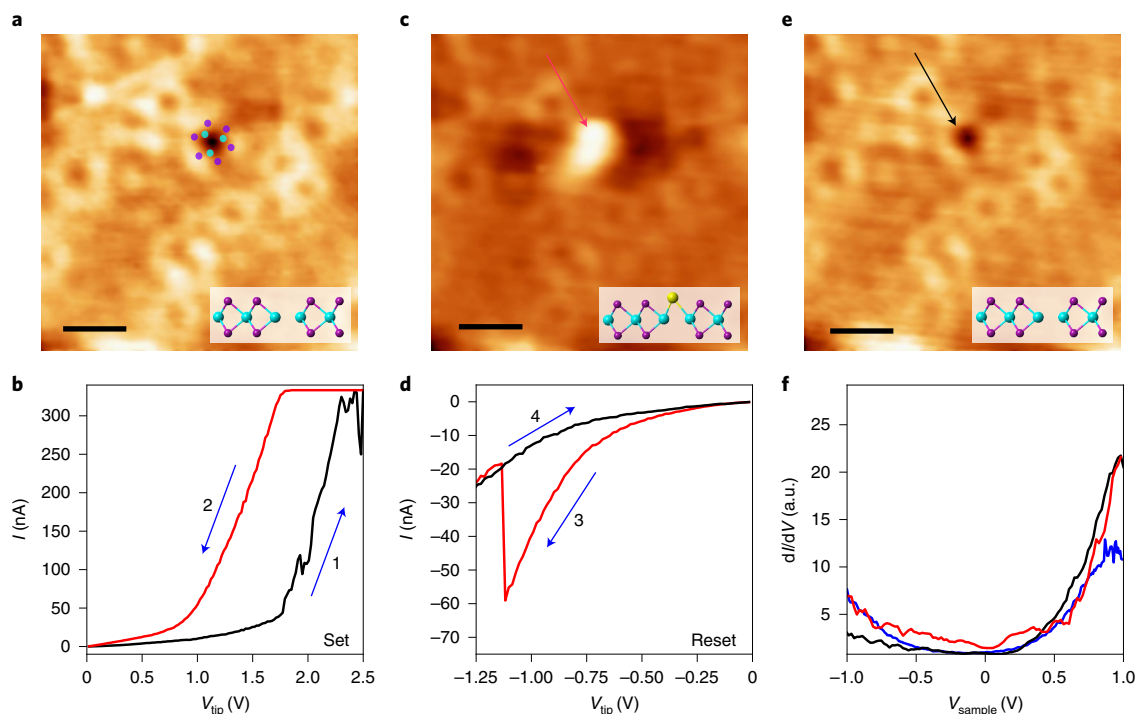


Fig. 3 | Atomistic observation of ‘set–reset’ sequences for V_{S_2} defects. **a**, STM image of the initial V_{S_2} point defect. Inset: cross-sectional view of the defect structure. Locations of sulfur and molybdenum atoms are shown in purple and cyan, respectively. **b**, A ‘set’ event induced by a voltage bias of -1.8 V. **c**, STM image of the same defect after the set event. The top sulfur site filled by a substitutational gold atom (yellow in inset) marked with the red arrow. **d**, A ‘reset’ event in the defect site. **e**, The defect structure returns to its original configuration (black arrow) after the reset event. **f**, STS measurements on the defect site before (black) and after (red) the substitution of the gold atom. Compared with the STS measurements taken far away from the defect site (blue curve) (tunnelling parameters: $V_{\text{sample}} = 0.7$ V; $I = 100$ pA). The blue arrows represent the direction and sequence of voltage sweeps in **b** and **d**. Scale bars, 1 nm.

formation energy, sulfur vacancies can still be created via the field-induced removal of S atoms by the STM tip at high bias voltages and reduced tip–sample distances²⁹. Similarly, substitutional gold defects have a binding energy of around -3 eV (refs. ^{30,31}) per gold atom, which is in the same range as that for the sulfur atom in the MoS_2 monolayer. Enhanced electric fields around the tip apex allow the migration of gold atoms to the defect sites or the removal of adsorbed species from them³², providing a stable platform for reversible operations. The current densities observed in single-defect memristors (of the order of 10^7 A cm⁻²) are comparable to mesoscopic-scale devices¹⁰ and well below the maximum current densities previously reported between an STM atomic contact and a metal surface³³. Furthermore, the density of sulfur vacancies can be globally altered by annealing the samples in a vacuum or S-rich atmospheres²². Therefore, MoS_2 monolayers and similar transitional metal dichalcogenides are an ideal platform for the energetically inexpensive controlled formation of vacancy defects to seed switching events.

In summary, we report a one-to-one correlation between resistive switching and metal adatom absorption at the vacancy defects of MoS_2 monolayers. Due to their inherent layered structure, MoS_2 provides a sharp, clean interface with metallic top and bottom electrodes that prevent excessive tunnelling currents even in the presence of vacancy defects. However, adatoms from the electrodes can be absorbed in these vacancy sites under a suitable electric field, resulting in a reversible change in the resistance of the MoS_2 MIM device. The reported resistance switching effect is expected to exist in similar 2D materials. The atomic-scale understanding and control of the resistive switching of a single defect represents the smallest memristor unit and paves the way for advanced memory

applications including ultra-dense storage and neuromorphic computing systems.

Online content

Any methods, additional references, Nature Research reporting summaries, source data, extended data, supplementary information, acknowledgements, peer review information; details of author contributions and competing interests; and statements of data and code availability are available at <https://doi.org/10.1038/s41565-020-00789-w>.

Received: 22 March 2020; Accepted: 1 October 2020;
Published online: 9 November 2020

References

- Chua, L. Memristor—the missing circuit element. *IEEE Trans. Circuit Theory* **18**, 507–519 (1971).
- Wong, H.-S. P. & Salahuddin, S. Memory leads the way to better computing. *Nat. Nanotechnol.* **10**, 191–194 (2015).
- Akinwande, D. et al. Graphene and two-dimensional materials for silicon technology. *Nature* **573**, 507–518 (2019).
- Wouters, D. J., Waser, R. & Wuttig, M. Phase-change and redox-based resistive switching memories. *Proc. IEEE* **103**, 1274–1288 (2015).
- Zhao, H. et al. Atomically thin femtojoule memristive device. *Adv. Mater.* **29**, 1703232 (2017).
- Wang, M. et al. Robust memristors based on layered two-dimensional materials. *Nat. Electron.* **1**, 130–136 (2018).
- Xu, R. et al. Vertical MoS_2 double-layer memristor with electrochemical metallization as an atomic-scale synapse with switching thresholds approaching 100 mV. *Nano Lett.* **19**, 2411–2417 (2019).
- Zhang, F. et al. Electric-field induced structural transition in vertical MoTe_2 - and $\text{Mo}_{1-x}\text{W}_x\text{Te}_2$ -based resistive memories. *Nat. Mater.* **18**, 55–61 (2019).

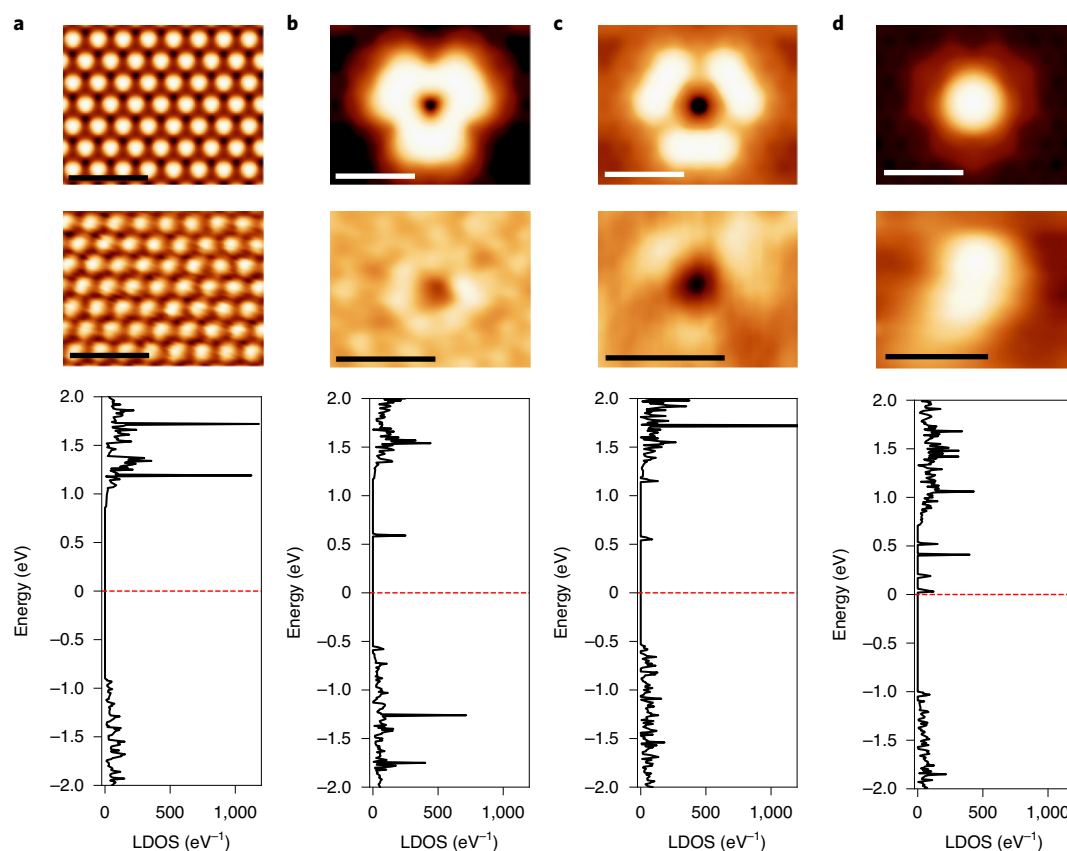


Fig. 4 | Atomistic defect simulations and spectral calculations for monolayer MoS₂. **a**, Pristine structure. **b**, V_S in the top layer. **c**, V_{S₂}. **d**, Gold substitution on the top V_{S₂} defect. Top: simulated STM images. Middle: experimental images for the corresponding defect structures. Bottom: calculated LDOS. Scale bars, 1 nm.

9. Sangwan, V. K. et al. Gate-tunable memristive phenomena mediated by grain boundaries in single-layer MoS₂. *Nat. Nanotechnol.* **10**, 403–406 (2015).
10. Ge, R. et al. Atomristor: nonvolatile resistance switching in atomic sheets of transition metal dichalcogenides. *Nano Lett.* **18**, 434–441 (2017).
11. Kim, M. et al. Zero-static power radio-frequency switches based on MoS₂ atomrystals. *Nat. Commun.* **9**, 2524 (2018).
12. Wu, X. et al. Thinnest nonvolatile memory based on monolayer h-BN. *Adv. Mater.* **31**, 1806790 (2019).
13. Ge, R. et al. Atomrystals: memory effect in atomically-thin sheets and record RF switches. *Proc. IEEE International Electron Devices Meeting (IEDM)* 22.6.1–22.6.4 (2018).
14. Valov, I., Waser, R., Jameson, J. R. & Kozicki, M. N. Electrochemical metallization memories—fundamentals, applications, prospects. *Nanotechnology* **22**, 254003 (2011).
15. Velicky, M. J. et al. Mechanism of gold-assisted exfoliation of centimeter-sized transition-metal dichalcogenide monolayers. *ACS Nano* **12**, 10463–10472 (2018).
16. Liu, Z. et al. Strain and structure heterogeneity in MoS₂ atomic layers grown by chemical vapour deposition. *Nat. Commun.* **5**, 5246 (2014).
17. Vancsó, P. et al. The intrinsic defect structure of exfoliated MoS₂ single layers revealed by scanning tunneling microscopy. *Sci. Rep.* **6**, 29726 (2016).
18. González, C., Biel, B. & Dappe, Y. J. Theoretical characterisation of point defects on a MoS₂ monolayer by scanning tunnelling microscopy. *Nanotechnology* **27**, 105702 (2016).
19. Zhou, W. et al. Intrinsic structural defects in monolayer molybdenum disulfide. *Nano Lett.* **13**, 2615–2622 (2013).
20. Zhang, C., Johnson, A., Hsu, C.-L., Li, L.-J. & Shih, C.-K. Direct imaging of band profile in single layer MoS₂ on graphite: quasiparticle energy gap, metallic edge states, and edge band bending. *Nano Lett.* **14**, 2443–2447 (2014).
21. Sørensen, S. G., Füchtbauer, H. G., Tuxen, A. K., Walton, A. S. & Lauritsen, J. V. Structure and electronic properties of in situ synthesized single-layer MoS₂ on a gold surface. *ACS Nano* **8**, 6788–6796 (2014).
22. Zhou, X. et al. Periodic modulation of the doping level in striped MoS₂ superstructures. *ACS Nano* **10**, 3461–3468 (2016).
23. Chiu, M.-H. et al. Determination of band alignment in the single-layer MoS₂/WSe₂ heterojunction. *Nat. Commun.* **6**, 7666 (2015).
24. Martinez-Castro, J. et al. Scanning tunneling microscopy of an air sensitive dichalcogenide through an encapsulating layer. *Nano Lett.* **18**, 6696–6702 (2018).
25. Song, S. H., Joo, M.-K., Neumann, M., Kim, H. & Lee, Y. H. Probing defect dynamics in monolayer MoS₂ via noise nanospectroscopy. *Nat. Commun.* **8**, 2121 (2017).
26. Ko, W. et al. Tip-induced local strain on MoS₂/graphite detected by inelastic electron tunneling spectroscopy. *Phys. Rev. B* **97**, 125401 (2018).
27. Marion, I. D. et al. Atomic-scale defects and electronic properties of a transferred synthesized MoS₂ monolayer. *Nanotechnology* **29**, 305703 (2018).
28. Hong, J. et al. Exploring atomic defects in molybdenum disulfide monolayers. *Nat. Commun.* **6**, 6293 (2015).
29. Huang, J. L., Sung, Y. E. & Lieber, C. M. Field-induced surface modification on the atomic scale by scanning tunneling microscopy. *Appl. Phys. Lett.* **61**, 1528–1530 (1992).
30. Miralrio, A., Cortes, E. R. & Castro, M. Electronic properties and enhanced reactivity of MoS₂ monolayers with substitutional gold atoms embedded into sulfur vacancies. *Appl. Surf. Sci.* **455**, 758–770 (2018).
31. Lin, Y. C. et al. Properties of individual dopant atoms in single-layer MoS₂: atomic structure, migration, and enhanced reactivity. *Adv. Mater.* **26**, 2857–2861 (2014).
32. Ko, W., Ma, C., Nguyen, G. D., Kolmer, M. & Li, A. P. Atomic-scale manipulation and in situ characterization with scanning tunneling microscopy. *Adv. Funct. Mater.* **29**, 1903770 (2019).
33. Scheer, E. et al. The signature of chemical valence in the electrical conduction through a single-atom contact. *Nature* **394**, 154–157 (1998).

Publisher's note Springer Nature remains neutral with regard to jurisdictional claims in published maps and institutional affiliations.

© The Author(s), under exclusive licence to Springer Nature Limited 2020

Methods

Sample preparation and STM measurements. Very-large-scale monolayer MoS₂ flakes were mechanically exfoliated on freshly deposited Au films (30 nm Au with 1 nm Ti adhesion layer) on 90 nm SiO₂/Si substrates as described previously¹⁵. The exfoliated MoS₂ could be easily identified with an optical camera that guided the STM tip on top of the monolayer regions for performing the imaging, spectroscopy and transport studies. Before the first set of STM measurements, the samples were annealed at a temperature of 250 °C for several hours in ultrahigh vacuum conditions (pressure less than 10⁻¹⁰ torr) to remove water and weakly bonded molecules. At this stage, we observed a small number of sulfur vacancy defects with a measured defect density of less than 10¹² cm⁻². Initial STM investigations were performed with gold or tungsten STM tips. The samples were later annealed at 400 °C to increase the sulfur vacancy density. Afterwards, STM and in situ transport measurements were performed with gold STM tips, which were etched using a 50% saturated KCl solution. All the STM measurements were performed with a variable-temperature STM system operated at 100 K. The quality and sharpness of the STM tips were tested with STM/STS measurements on a clean Au(111) surface before being used on the MoS₂ surface. For the STS measurements, a modulation signal of 20 mV at 1 KHz was used.

Before each transport measurement, the gold STM tip was fixed on the surface using a stabilization voltage within the bandgap of MoS₂ to ensure a reduced vacuum gap between the tip and MoS₂ surface. Then, the STM tip was further approached to the surface to provide a stable mechanical and electrical contact. The high mechanical strength of MoS₂ prevented any damage to the tip and the sample during the physical contact²⁶. For transport measurements, a compliance current of 3.3 nA or 330 nA was used. To protect the MoS₂ monolayers and tip apex from irreversible modifications, the transport experiments were first performed with a low compliance current. If a switching event is not observed, the compliance current was increased, and the measurements were repeated. STM and transport studies were performed in atomically flat and clean regions away from the mesoscopic-scale inhomogeneities of MoS₂ and the underlying gold film.

Raman spectroscopy and PL measurements. Raman spectroscopy and PL measurements were performed in ambient conditions on a Renishaw inVia system using a 532 nm wavelength source. The typical spot size of the laser beam was around 1.5 μm. While the MoS₂ regions are much larger than the spot size, the size of the randomly oriented gold grains is limited to tens of nanometres due to the thin-film growth on the amorphous SiO₂ surface. The granular structure of the underlying gold film creates local variations in the Au–MoS₂ interface and the local strain of the MoS₂ monolayers, which broadens both PL and Raman peaks. Due to the suppression in PL, signal integration times of up to 30 min were required to obtain the reported PL spectra.

Computational methods. To simulate the STM images of a single sulfur vacancy, double sulfur vacancy and gold atom adsorbed on top of the vacancy site in monolayer MoS₂, we carried out plane-wave density functional theory calculations by using the Vienna ab initio simulation package³⁴. Projector augmented-wave pseudopotentials were used for electron–ion interactions, and the generalized gradient approximation with the Perdew–Burke–Ernzerhof functional³⁵ was adopted for the exchange–correlation interactions. Monolayer MoS₂ was modelled by periodic slab geometry, where a vacuum separation of 21 Å in the out-of-plane direction (z direction) was used to avoid spurious interactions between the periodic images. An 8 × 8 supercell of monolayer MoS₂ (in-plane lattice constant, ~25.51 Å) was built to model the sulfur vacancies and gold atom adsorption, where all the atoms were relaxed until the residual forces were below 0.01 eV Å⁻¹. The plane-wave cutoff energy was set at 280 eV, and 3 × 3 × 1 k-point sampling was used. Based on the optimized structures, we then obtained the partial charge density from VASP for a specific electronic band or at a specific bias energy. Finally, constant-current STM topographic images were computed using the converged partial charge densities within the Tersoff–Hamann approximation³⁶.

For transport calculations, a small piece of MoS₂ sheet is used in an MIM structure comprising two Au(111) outer layers. Two MIM structures of

Au–MoS₂–Au with and without gold adsorption were optimized by the ab initio tool, QuantumWise 2017.2. The first-principles calculations were performed using Kohn–Sham density functional theory³⁷ with generalized gradient approximation for the exchange and correlation interactions. To minimize the computational cost while ensuring accuracy, 50 Hartree is set as the mesh-cutoff energy and 10 × 5 × 1 k-points are sampled in the Brillouin zone. The semi-empirical dispersion potential, DFT-D2, is added to describe the van der Waals forces. Both MIM structures are optimized until the atomistic force is below 0.03 eV Å⁻¹. Subsequently, the standard non-equilibrium Green's function is used to compute the *I*–*V* characteristics of both structures.

Data availability

The authors declare that the main data supporting the findings of this study are available within the Letter and its Supplementary Information. Extra data are available from the corresponding author upon reasonable request. Source data are provided with this paper.

References

- Kresse, G. & Furthmüller, J. Efficiency of ab-initio total energy calculations for metals and semiconductors using a plane-wave basis set. *Comput. Mater. Sci.* **6**, 15–50 (1996).
- Perdew, J. P., Burke, K. & Ernzerhof, M. Generalized gradient approximation made simple. *Phys. Rev. Lett.* **77**, 3865–3868 (1996).
- Tersoff, J. & Hamann, D. R. Theory of the scanning tunneling microscope. *Phys. Rev. B* **31**, 805–813 (1985).
- Kohn, W. & Sham, L. J. Self-consistent equations including exchange and correlation effects. *Phys. Rev.* **140**, A1133–A1138 (1965).

Acknowledgements

This work was supported in part by the Presidential Early Career Award for Scientists and Engineers (PECASE) through the Army Research Office (W911NF-16-1-0277), and a National Science Foundation grant (ECCS-1809017). S.M.H. acknowledges support from a US S&T Cooperation Program. The facilities of the Center for Dynamics and Control of Materials: an NSF Materials Research Science and Engineering Center (MRSEC) was used for materials characterization. A portion of this research, including STM, transport measurements and STM simulations, was conducted at the Center for Nanophase Materials Sciences at Oak Ridge National Laboratory, which is a US Department of Energy User Facility. We thank W. R. Hendren and R. M. Bowman for their help with the metal film deposition.

Author contributions

S.M.H. conducted the STM and transport measurements with the help of W.K. R.G. carried out the Raman spectroscopy and PL measurements. G.E.D. and F.H. prepared the large-scale exfoliated monolayer MoS₂ samples. P.-A.C. and L.L. performed the atomistic simulations. S.M.H. and D.A. initiated the research on the atomistic origins of non-volatile resistance switching in single-layer atomic sheets. M.-H.C., A.-P.L. and D.A. coordinated and supervised the research. All authors contributed to the article based on the draft written by S.M.H. and D.A.

Competing interests

The authors declare no competing interests.

Additional information

Supplementary information is available for this paper at <https://doi.org/10.1038/s41565-020-00789-w>.

Correspondence and requests for materials should be addressed to D.A.

Peer review information *Nature Nanotechnology* thanks Hyeon-Jin Shin and the other, anonymous, reviewer(s) for their contribution to the peer review of this work.

Reprints and permissions information is available at www.nature.com/reprints.

Terms and Conditions

Springer Nature journal content, brought to you courtesy of Springer Nature Customer Service Center GmbH (“Springer Nature”).

Springer Nature supports a reasonable amount of sharing of research papers by authors, subscribers and authorised users (“Users”), for small-scale personal, non-commercial use provided that all copyright, trade and service marks and other proprietary notices are maintained. By accessing, sharing, receiving or otherwise using the Springer Nature journal content you agree to these terms of use (“Terms”). For these purposes, Springer Nature considers academic use (by researchers and students) to be non-commercial.

These Terms are supplementary and will apply in addition to any applicable website terms and conditions, a relevant site licence or a personal subscription. These Terms will prevail over any conflict or ambiguity with regards to the relevant terms, a site licence or a personal subscription (to the extent of the conflict or ambiguity only). For Creative Commons-licensed articles, the terms of the Creative Commons license used will apply.

We collect and use personal data to provide access to the Springer Nature journal content. We may also use these personal data internally within ResearchGate and Springer Nature and as agreed share it, in an anonymised way, for purposes of tracking, analysis and reporting. We will not otherwise disclose your personal data outside the ResearchGate or the Springer Nature group of companies unless we have your permission as detailed in the Privacy Policy.

While Users may use the Springer Nature journal content for small scale, personal non-commercial use, it is important to note that Users may not:

1. use such content for the purpose of providing other users with access on a regular or large scale basis or as a means to circumvent access control;
2. use such content where to do so would be considered a criminal or statutory offence in any jurisdiction, or gives rise to civil liability, or is otherwise unlawful;
3. falsely or misleadingly imply or suggest endorsement, approval, sponsorship, or association unless explicitly agreed to by Springer Nature in writing;
4. use bots or other automated methods to access the content or redirect messages
5. override any security feature or exclusionary protocol; or
6. share the content in order to create substitute for Springer Nature products or services or a systematic database of Springer Nature journal content.

In line with the restriction against commercial use, Springer Nature does not permit the creation of a product or service that creates revenue, royalties, rent or income from our content or its inclusion as part of a paid for service or for other commercial gain. Springer Nature journal content cannot be used for inter-library loans and librarians may not upload Springer Nature journal content on a large scale into their, or any other, institutional repository.

These terms of use are reviewed regularly and may be amended at any time. Springer Nature is not obligated to publish any information or content on this website and may remove it or features or functionality at our sole discretion, at any time with or without notice. Springer Nature may revoke this licence to you at any time and remove access to any copies of the Springer Nature journal content which have been saved.

To the fullest extent permitted by law, Springer Nature makes no warranties, representations or guarantees to Users, either express or implied with respect to the Springer nature journal content and all parties disclaim and waive any implied warranties or warranties imposed by law, including merchantability or fitness for any particular purpose.

Please note that these rights do not automatically extend to content, data or other material published by Springer Nature that may be licensed from third parties.

If you would like to use or distribute our Springer Nature journal content to a wider audience or on a regular basis or in any other manner not expressly permitted by these Terms, please contact Springer Nature at

onlineservice@springernature.com